


RESEARCH

Open Access



# Ultrafast modulation of valley dynamics in multiple $WS_2$ – Ag gratings strong coupling system

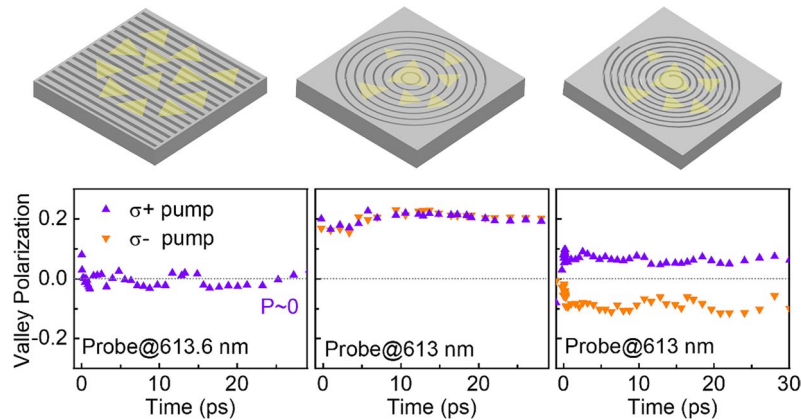
Le-Yi Zhao<sup>1,2</sup>, Hai Wang<sup>1\*</sup>, Hai-Yu Wang<sup>1\*</sup>, Qiang Zhou<sup>2\*</sup>, Xu-Lin Zhang<sup>1</sup>, Tong Cui<sup>3</sup>, Lei Wang<sup>1</sup>, Tian-Yu Liu<sup>1</sup>, Yu-Xiao Han<sup>3</sup>, Yang Luo<sup>1</sup>, Yuan-Yuan Yue<sup>1</sup>, Mu-Sen Song<sup>1</sup> and Hong-Bo Sun<sup>1,3</sup> 

\*Correspondence: wanghai03@jlu.edu.cn; haiyu\_wang@jlu.edu.cn; zhouqiang@jlu.edu.cn  
<sup>1</sup> State Key Laboratory of Integrated Optoelectronics, College of Electronic Science and Engineering, Jilin University, Changchun 130012, China  
<sup>2</sup> State Key Laboratory of Superhard Materials, College of Physics, Jilin University, Changchun 130012, China  
Full list of author information is available at the end of the article

## Abstract

Strong light-matter interactions in two-dimensional transition metal dichalcogenides (TMDCs) with robust spin-valley degrees of freedom open up the prospect of valleytronic devices. A thorough understanding on the dynamics of the valley polarizations in the strong coupling regime is urgently required. Here, multiple polarized TMDCs-SPPs hybrid systems were constructed by combining monolayer  $WS_2$  flakes to linear, circular, and spiral Ag gratings, resulting in linear and circular polarized modulation on the coherent hybrid states, respectively. Particularly, valley polaritons can be tailored asymmetrically by chiral strong coupling regime. Furthermore, the dynamics of the polarized polaritons were directly analyzed by transient absorption (TA) measurement. Both of the linear and circular polarization difference in the TA spectra can be retained for a remarkable long time, leading to a polarized PL even at room temperature. More importantly, in the chiral strong coupled  $WS_2$ -spiral Ag grating devices, the mechanism of the asymmetrical valley-polarized PL ( $p_{\sigma_+} = 14.9\%$  and  $p_{\sigma_-} = 10.8\%$ ) is proved by the opposite valley polarization dynamics in the circularly polarized TA spectra. The multiple polarization modulation in monolayer TMDCs-SPPs strong coupling devices could provide a viable route toward multiple polarization polaritonic devices.

**Keywords:** Strong coupling, Polarization, Valley dynamics, Surface plasmon polaritons, Transition metal dichalcogenides



## Introduction

Compared with traditional semiconductors, two-dimensional transition metal dichalcogenides (TMDCs) with the excellent optical [1, 2], electronic [3, 4] and valley pseudospin properties [5–8], have shown various important applications in optical switching [9], high-speed transistors [10, 11], and quantum information processing [12]. Furthermore, because the lattice-match condition is not required, TMDCs are easy to manipulate into functional devices with stacking processes [13]. Additionally, compared to bulk materials, monolayer TMDCs with reduced dielectric screening and strong quantum confinement [14, 15] has become one of the most preferred candidates for the research of light-matter interaction.

According to the energy exchange rate between the light and matter component, two kinds of light-matter coupling regimes can be identified. One is weak coupling regime [16], in which the excitation energy lost rapidly and can't be oscillated between the oscillators. In this regime, significant enhancement of fluorescence is afforded by Purcell effect, which is the most used method to make up the disadvantages of low quantum efficiency (typically less than 1%) of monolayer TMDCs [17]. In contrast, the excitation energy can be exchanged back and forth between light and matter in strong coupling regime, where the rate of the exchange is faster than any decoherent process, leading to the formation of hybrid light-matter states, called polaritons. As a half-light and half-matter hybrid system, the polaritons not only have the advantages of light, such as small effective mass, fast propagation, long-term spatiotemporal coherence, etc., but also have the remarkable properties inherited from matter fraction, such as strong interaction and nonlinearities. Combining these advantages, strong coupling hybrid states have suggested many applications including Bose–Einstein condensation [18, 19], low-threshold polariton lasing [20, 21] and long-range energy transfer mobility [22].

Recently, light-matter interaction [23] has been extensively studied on monolayer TMDCs coupled with electromagnetic fields confined in microcavities [24–26] or surface plasmon polaritons (SPPs) [27–31]. Importantly, as excellent valleytronic materials, great interest has been focused on TMDCs, in which valley degree of freedom can be directly addressed under strong coupling regime [24]. In multiple experiments, it has been demonstrated that valley polarization can be retained even in ambient conditions by coupling TMDCs to optical microcavity [24, 32, 33]. On the other hand, plasmonic

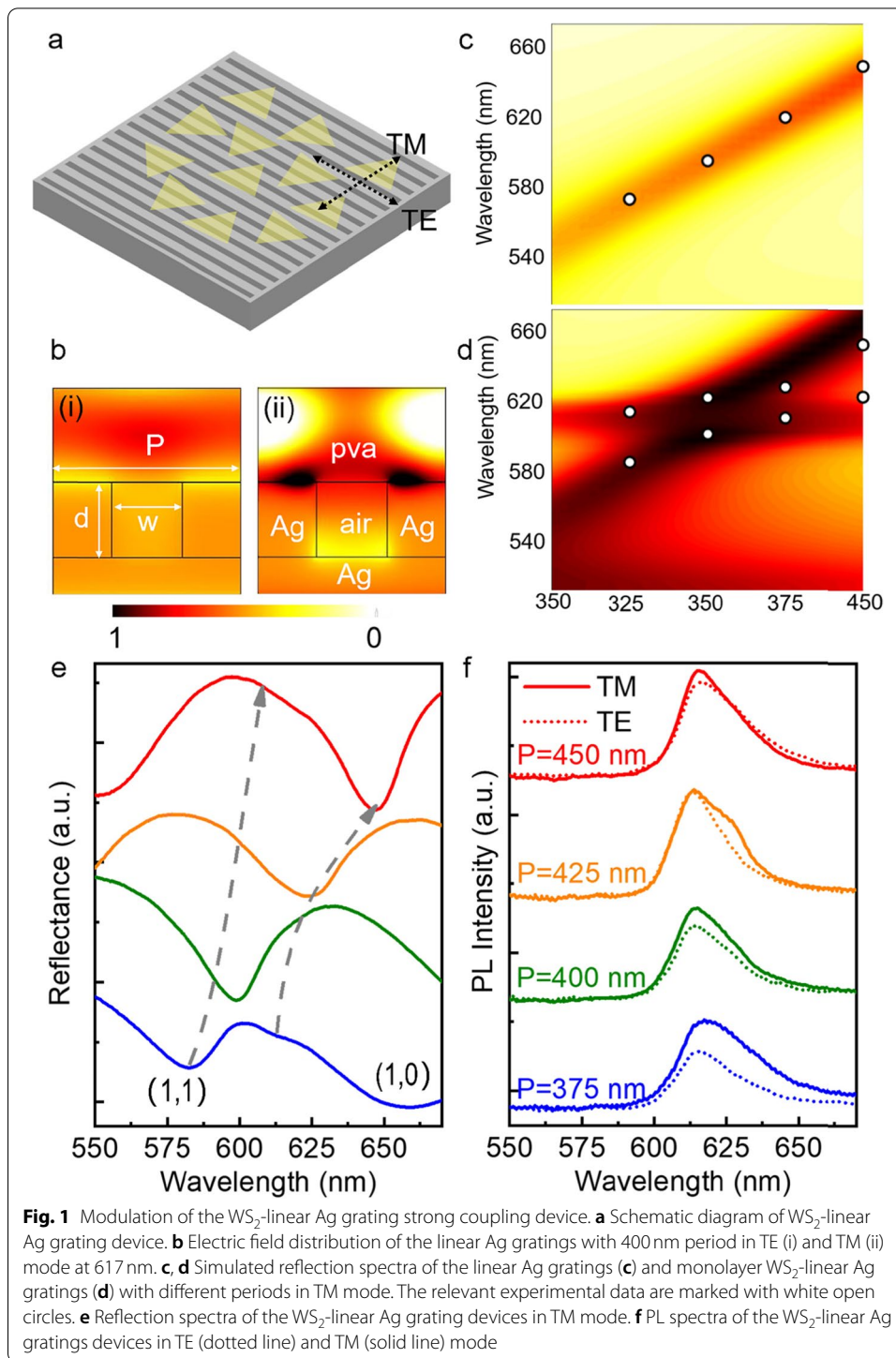
nanostructures, as another solution to confine light, can also be used to couple with TMDCs [34–36]. Particularly, SPPs have the advantages of being capable of flexible design and opening to environment [37, 38]. These peculiarities offer a better platform for polarization modulation [39–43], especially for valley pseudospin control [35, 36]. For example, Shi et al. report that a linear polarized second-harmonic generation can be achieved by coupling WS<sub>2</sub> to Ag nanogroove gratings [43]. Besides, precisely designed plasmonic chiral resonators have been used to successfully control valley-polarized PL emission [35, 44–48]. Especially, Hu's work successfully achieved the modulation of the nonlinear valley–exciton-locked emission in any direction in free space [35]. However, until now valley dynamics in the strong coupling regime have not been reported yet. In particular, little is known about the valley depolarization mechanism in the TMDCs-SPPs coherent hybrid system.

In this work, we demonstrate that strong TMDCs-SPPs coupling can be achieved by combining triangular monolayer WS<sub>2</sub> to linear, circular, and spiral Ag gratings, in which the mechanism of linear and circular polarized modulation on the exciton-polaritons is revealed by the ultrafast pump-probe approach. In the strong coupling regime, the difference of the polarized TA spectra can be retained for an extremely long time, which were measured in both WS<sub>2</sub>-linear and circular Ag gratings devices. Particularly, an asymmetrical valley-polarized PL ( $P_{\sigma+} = 14.9\%$  and  $P_{\sigma-} = 10.8\%$ ) is clearly shown in the WS<sub>2</sub>-spiral Ag grating device at room temperature, behavior associated to a long kept asymmetric valley polarization in the chiral strong coupling regime. These multiple polarized strong coupling WS<sub>2</sub>-Ag grating devices could provide new opportunities in the manipulation of information processing and communication.

## Result and discussion

The devices used in this work were all fabricated by a series of nano-processing steps on silicon substrate (see [Methods](#) for details). The WS<sub>2</sub>-linear Ag gratings devices were first studied and their schematic is shown in Fig. 1a. The lattice periods ( $p$ ) varied from 375 nm to 450 nm, while the groove width ( $w$ ) and depth ( $d$ ) was kept at 150 nm and 160 nm. According to the cross-sectional image shown in Fig. S4, the side wall of the gratings is nearly vertical and the surface of the sample is smooth enough. The triangular monolayer WS<sub>2</sub> flakes were transferred on the top of the linear Ag gratings through a wet transfer method (see Fig. S2 in Supporting Information). According to the Raman spectra of the WS<sub>2</sub>-Ag gratings device as shown in Fig. S5, there is no tension to the triangular monolayer WS<sub>2</sub> on the surface of the gratings. Before the transfer, a 5 nm aluminum oxide (Al<sub>2</sub>O<sub>3</sub>) was evaporated on the Ag film to avoid fluorescence quenching. Particularly, because the Al<sub>2</sub>O<sub>3</sub> film is thin enough, the monolayer WS<sub>2</sub> is still in the maximum field of the enhancement area. Finally, a 300 nm thick polyvinyl alcohol (PVA) film was spin-coated onto the devices, resulting in the SPPs resonance can be tuned to the location of the A exciton of monolayer WS<sub>2</sub>. In addition, the PVA layer can also protect the devices away from oxidation in the air environment.

Figure 1b illustrates the simulated electric field distribution of the linear Ag gratings with 400 nm period for excitation at 617 nm. Here, we refer to a TM (TE) mode when the polarization of the light is perpendicular (parallel) to the grating pitch. As can be seen, the strong SPPs fields can only be excited by TM polarized light and



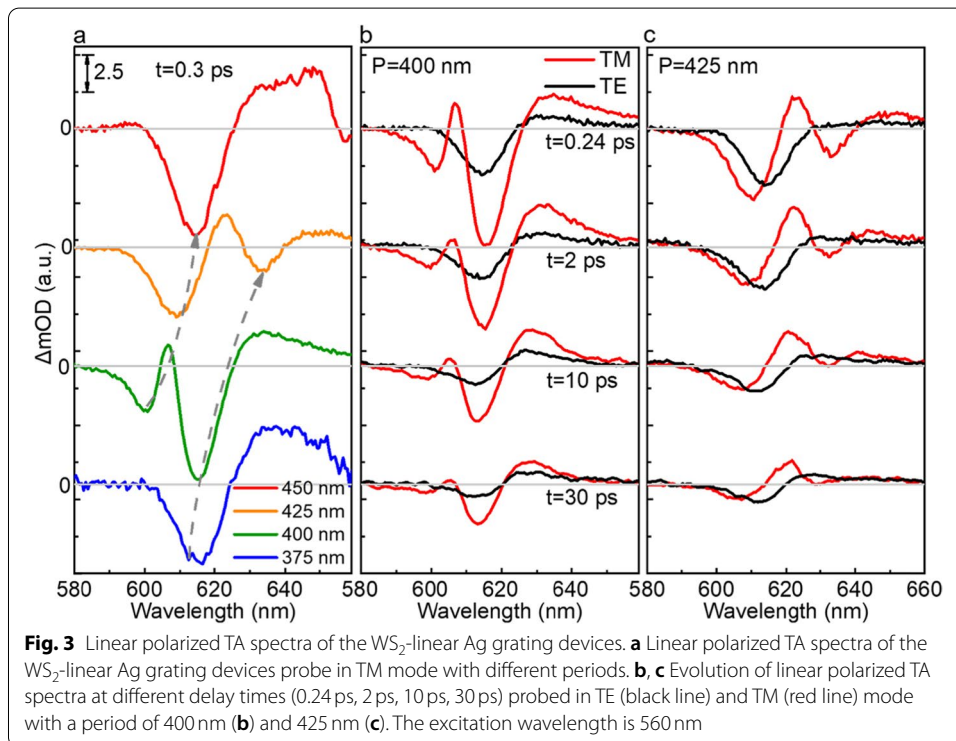
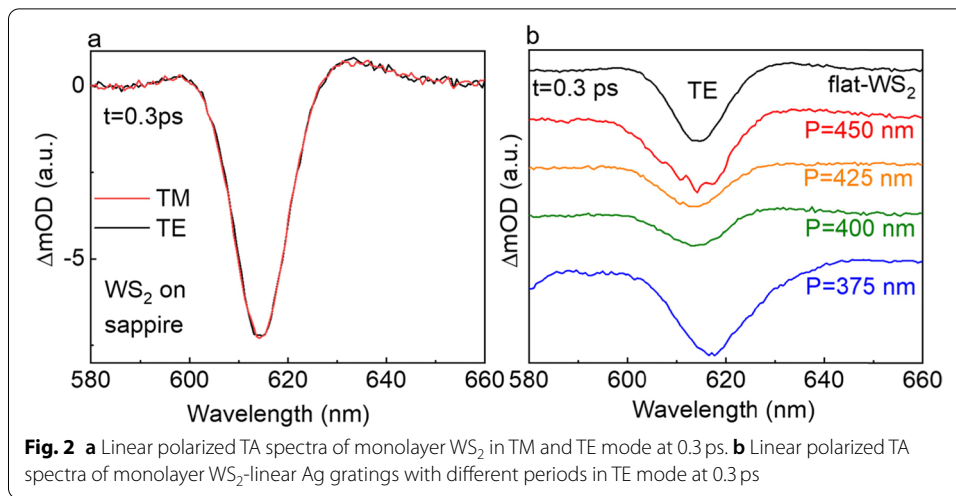
localized near the edge of the slit. Then the linear polarized reflection spectra in TM mode were calculated from the linear Ag gratings without and with monolayer  $WS_2$ , in Fig. 1c-d, which is consistent with the experimentally measured reflection spectra as shown in Fig. 1e. It is noted that the A exciton transition energy of  $WS_2$  and the SPPs

modes slightly split into two new hybrid states, whose peaks with the anti-crossing behavior show the evidence of strong coupling in TM mode.

To further display the linear polarized strong coupling in the hybrid WS<sub>2</sub>-linear Ag grating devices, linear polarized PL spectra were measured (Fig. 1f). The devices were excited by a 532 nm laser in TM mode, while the PL spectra were collected along TM and TE, respectively. For reference, monolayer WS<sub>2</sub> on flat Si shows a negligible linear-polarized emission according to previous report [49]. With respect to bare WS<sub>2</sub>, the PL spectra from the hybrid devices exhibit distinct differences in TM and TE mode. In addition, the linear-polarized emission of the hybrid devices can be modulated by tailoring the periods of the Ag gratings. At the period of 375 nm, both the (1,1) and (1,0) SPPs resonance peaks of the linear Ag grating have overlap parts with the A exciton of monolayer WS<sub>2</sub>, leading to stronger Purcell effect along the TM mode. Thus, it seems to have the largest difference between the TE and TM mode. However, the peaks of the two SPPs modes can't match the A exciton of monolayer WS<sub>2</sub>. Weak coupling still plays a dominant role in this device. Hence, in this case, the shape of the PL spectrum keeps the same shape under TE and TM mode. When the period increases to 400 and 425 nm, the SPPs resonance peak will red-shift and can overlap with the A exciton of monolayer WS<sub>2</sub>, thus maximizing the coupling strength. Under this condition, the shape of the PL spectra under TE and TM modes show significant difference. Compared with TE mode, a shoulder emission peak at 627 nm corresponding to the lower band appeared in TM mode, which further reveals that the polarized strong coupling can be achieved. As the period further increases, the SPPs resonance peak of the Ag gratings will shift out of the A exciton of monolayer WS<sub>2</sub>. Hence, the PL emission from the hybrid WS<sub>2</sub>-linear Ag grating device with the period of 450 nm shows slight differences between the TE and TM mode. Above all, only in TM mode, the shape of the linear-polarized PL emission spectra can be tailored in the WS<sub>2</sub>-linear Ag grating coupling devices, which indicated that polarized strong coupling can be modulated by the orientation of the gratings.

Although the steady-state reflection and PL spectra has proved that the linear polarized strong coupling can be achieved in the WS<sub>2</sub>-linear Ag grating devices. The photophysics of the polarized hybrid devices still needs to be clarified. In order to further understand the dynamics of the linear polarized strong coupling, transient absorption (TA) spectra [50] were carried out based on a 100 fs Ti-sapphire amplifier system (see [Methods](#) for details). In particular, the pump beam was always kept in TM mode, while the broad white light was set in TM or TE mode to realize linear polarized TA measurement. Thus, more information of the excited state in the hybrid devices can be reflected by the variation of the optical density ( $\Delta OD = OD_{\text{pump}} - OD_{\text{without pump}}$ ).

The reference sample with bare monolayer WS<sub>2</sub> on flat Ag film was first pumped by a 560 nm laser pulse. Figure 2a shows the TA spectra recorded immediately after the initial excitation at 0.3 ps. The TA spectra showed similar behavior under TM and TE mode probe. The narrow negative signal at around 610 nm was the ground state bleaching (GSB) signal. And the positive signal at 630 nm was attribute to excited state absorption. The TA experiments performed on the hybrid devices with different periods were also pump at 560 nm in TM mode. With respect to the reference sample, the TA spectra from the devices with different periods show similar behaviors under TE probe as shown in Fig. 2b. By contrast, totally different transient features are recorded in the TM probe.



As shown in Fig. 3a, two distinctive negative bands associated with the new hybrid SPPs-exciton states are observed. In addition, by varying the grating periods, the two peaks simultaneously red shift with increasing the period. Compared with steady-static measurements, TA spectra probed in TM mode give clearer characteristic of strong coupling: anti-crossing of energies. A Rabi splitting up to 50 meV can be achieved. These results indicate that linear-polarized coherent SPPs-exciton hybrid states can form in the hybrid devices.

Specifically, for the optimal coupling devices with periods of 400 nm and 425 nm, the TA spectra evolution probed in TM and TE mode are compared in Fig. 3b-c. As can be

seen, the two distinctive bands corresponding to the hybrid states in TM mode probe can be retained for a long time. Namely, the lifetime of the coherent hybrid states can be extremely long, which is consistent with previous reports [51, 52]. Hence, such unique anisotropic features in the WS<sub>2</sub>-linear Ag gratings devices should provide important applications in the linear polarization-modulated optical encoding technique [43].

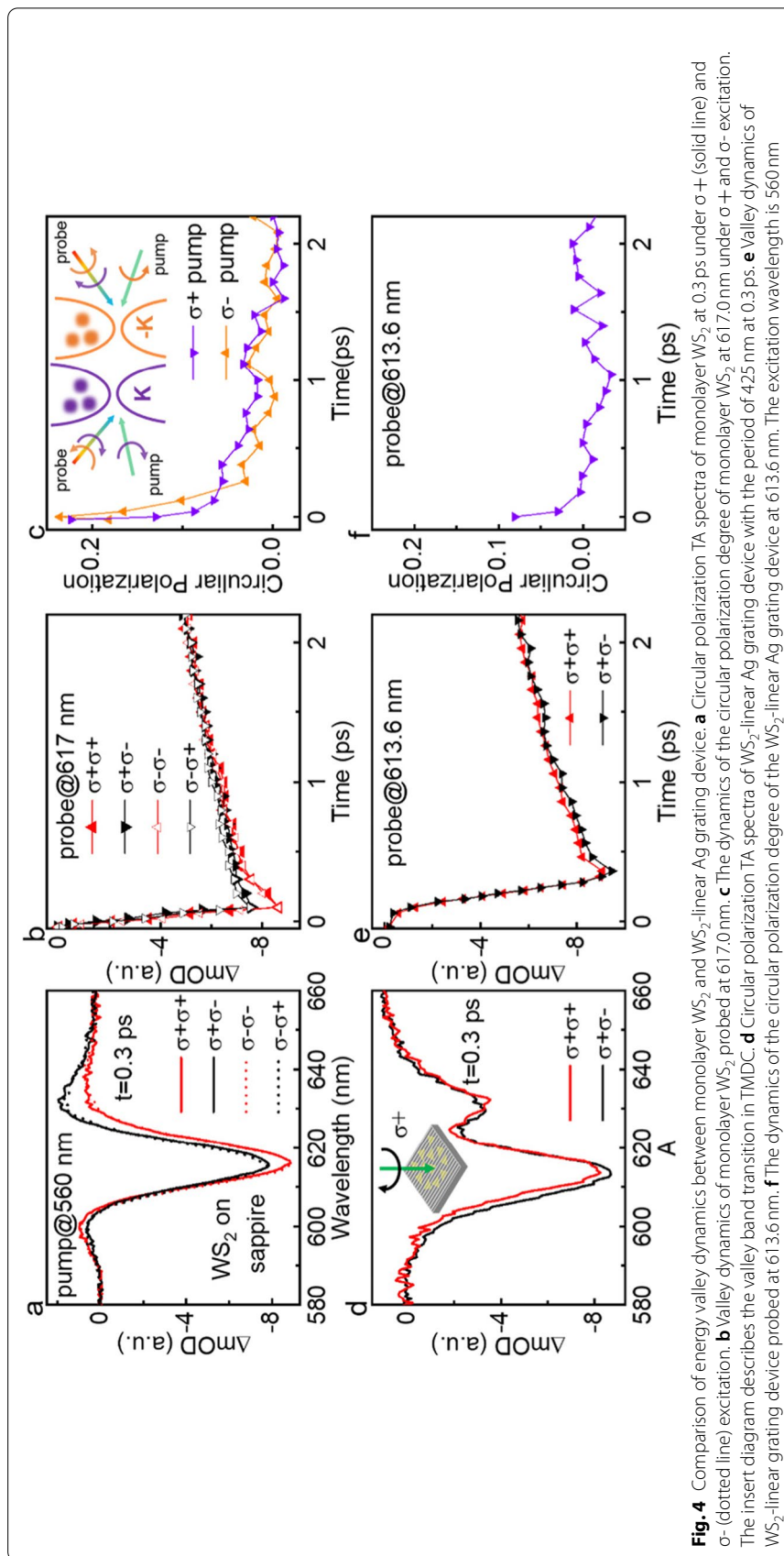
In addition to the modulation on linear polarization, the control on circular polarization is also of great significance due to the existence of energy valley in monolayer TMDCs. valley band transition in TMDC was illustrated in the insert diagram in Fig. 4c. It has been demonstrated that the valley pseudospin can be retained even at room temperature by coupling TMDCs to microcavities [24, 32, 33]. Namely the robustness of the valley pseudospin can be improved in strong coupling regime. Thus, to clarify whether the TMDCs-SPPs hybrid states can play the same role in valley polarization modulation, we further carried out circular polarized TA spectroscopy, in which the pump and probe light was set as left ( $\sigma+$ ) or right ( $\sigma-$ ) circular polarization by adding a quarter wave plate into the light path.

As a reference, the monolayer WS<sub>2</sub> on flat Ag film was also first measured. The initial TA spectra at 0.3 ps with different pump-probe configurations were plotted in Fig. 4a, in which the maximum differences between the same (SCP) and opposite (OCP) circular polarization of the pump and probe pulses are recorded. The prominent distinction of the SCP and OCP spectra are located at the red-side of the GSB and the photoinduced absorption (PIA) signal at 630 nm, which can be attribute to the energy band renormalization originating from the coulomb-induced intervalley scattering [53]. Then we compared the valley dynamics at the GBS peak (617 nm) under SCP and OCP probe in Fig. 4b. It can be seen that the differences between the SCP and OCP signal disappeared within a very short time due to the fast intervalley scattering effect. The differences of the valley dynamic can be characterized by circular polarization degree (P):

$$P_{\sigma+} = \frac{\Delta OD_{++} - \Delta OD_{+-}}{\Delta OD_{++} + \Delta OD_{+-}} \quad \text{or} \quad P_{\sigma-} = \frac{\Delta OD_{--} - \Delta OD_{-+}}{\Delta OD_{--} + \Delta OD_{-+}} \quad (1)$$

where  $\Delta OD_{++}$  ( $\Delta OD_{--}$ ) and  $\Delta OD_{+-}$  ( $\Delta OD_{-+}$ ) refer to the SCP and OCP probe signals under  $\sigma+$  ( $\sigma-$ ) excitation. As illustrated in Fig. 4c, the valley polarization for monolayer WS<sub>2</sub> has a very short lifetime  $\sim 650$  fs, which is consistent with the previous report. Besides, it's also worth noticing that the kinetics of the circular polarizability curve excited by  $\sigma+$  light almost coincide with that excited by the  $\sigma-$  light, which suggests that the K and -K energy valleys are symmetric in monolayer WS<sub>2</sub>.

More importantly, the circular polarized TA spectra were performed on the WS<sub>2</sub>-linear Ag gratings devices. Two distinctive bands assigned to the hybrid states were plotted in Fig. 4d, which demonstrate that strong coupling regime can still be achieved under circular light excitation. But the difference of the TA spectra under SCP and OCP probe is almost negligible even at the initial time. As shown in Fig. 4e, the valley dynamics of the upper band peak also show the same behavior under SCP and OCP probe, leading to a zero circular polarization degree over time (Fig. 4f). Thus, we can conclude that the valley polarization cannot be distinguished in the strong coupled WS<sub>2</sub>-linear Ag grating devices. In fact, the linear Ag gratings can be considered as a wire-grid polarizer [54, 55], which can convert circularly polarized light into linearly polarized light once the pump



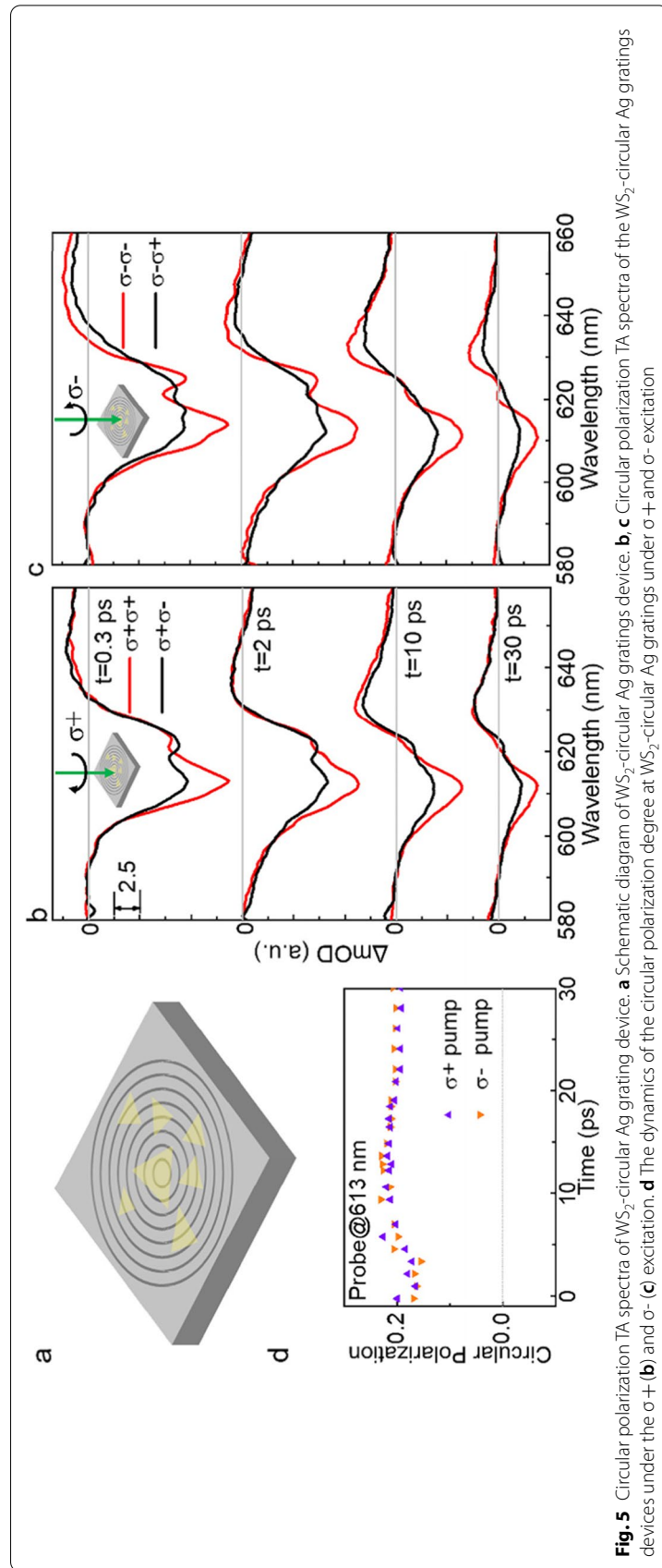


light hits on the hybrid devices, resulting in excitons generated in both K and -K valleys without valley polarization. The simulated circular polarized steady state spectrum of the linear Ag grating in Fig. S6 can also explain this.

Since the linear Ag gratings cannot be directly used in valley modulation, we further designed circular gratings to couple with monolayer WS<sub>2</sub>. The circular gratings can not only provide an enhanced electric field, but also increase the circular polarization degree of the SPPs as demonstrated in Clara's work [56]. Figure 5a exhibits the schematic of the WS<sub>2</sub>-circular Ag gratings device, which was fabricated by the same procedure. The radius of the innermost circular ring is 150 nm, while the groove width and the spiral pitch are set as 80 and 400 nm, respectively.

Once again, the circular polarized TA experiments were still carried out by a 560 nm pump laser. The excitation position was chosen at the center of the circular gratings to maximize the coupling intensity. The evolution of the spectra for the WS<sub>2</sub>-Circular Ag gratings devices are reported in Fig. 5b-c illustrating two GSB signals in all the pump-probe configurations. Even though the separation of the two peaks is not obvious as that measured from the WS<sub>2</sub>-linear Ag gratings devices, we can still argue that the system is dominated by strong coupling regime. Importantly, significant differences in the SCP and OCP spectra can be distinguished and retained for an extremely long time. Especially, the dynamics of the circular polarization degree with the maximum value at the peak of the upper band (613 nm) were plotted in Fig. 5d. As can be seen, the circular polarization degree can be kept around 20% over a long time under both  $\sigma+$  or  $\sigma-$  excitation. Hence, we demonstrated that significant enhancement of the valley polarization lifetime can be achieved under strong coupling regime in the WS<sub>2</sub>-Circular Ag gratings devices. Such a feature is of considerable importance for potential applications in valleytronics. In addition, another should be noted is that the GSB signals in the SCP spectra is always bigger than that in OCP spectra, resulting in a positive circular polarization degree under both  $\sigma+$  and  $\sigma-$  excitation as shown in Fig. 5d. In other words, owing to the symmetry of the circular gratings, the modulation on the two valleys is still equivalent under  $\sigma+$  and  $\sigma-$  excitation, which is also consistent with the simulated circularly polarized steady state spectrum of the circular Ag grating in Fig. S6.

It is well known that the  $\sigma+$  and  $\sigma-$  circular polarization light can be selectively enhanced by right-hand or left-hand structures [44, 46, 48, 56], such as a plasmonic Archimedean spiral. Rather than enhancing valley spin lifetime, spirals with asymmetry of structures would provide a better platform for improve the valley-addressable ability [56]. In the next step, we focus on valley modulation under strong coupling with chiral plasmonic structures. The circular Ag grating was replaced by a clockwise spiral grating to couple with monolayer WS<sub>2</sub> as the schematic diagram shown in Fig. 6a. The start radius of the spiral is set to 150 nm, while the groove width and the spiral pitch are still set as 80 and 400 nm, respectively. First, the circular dichroism (CD) spectra were measured to reveal the differential response from the bare spiral Ag gratings between  $\sigma+$  and  $\sigma-$  light. Here, the CD spectra is calculated with:  $CD = R(\sigma+) - R(\sigma-)$ , where  $R(\sigma+)$  and  $R(\sigma-)$  are the reflection spectra from the devices. As shown in Fig. 6b, there is no obvious chiral light response at the flat Ag film and the circular Ag gratings. While for the spiral Ag gratings, the CD spectrum shows a strong chiral light response around 617 nm as the black curve depicted,



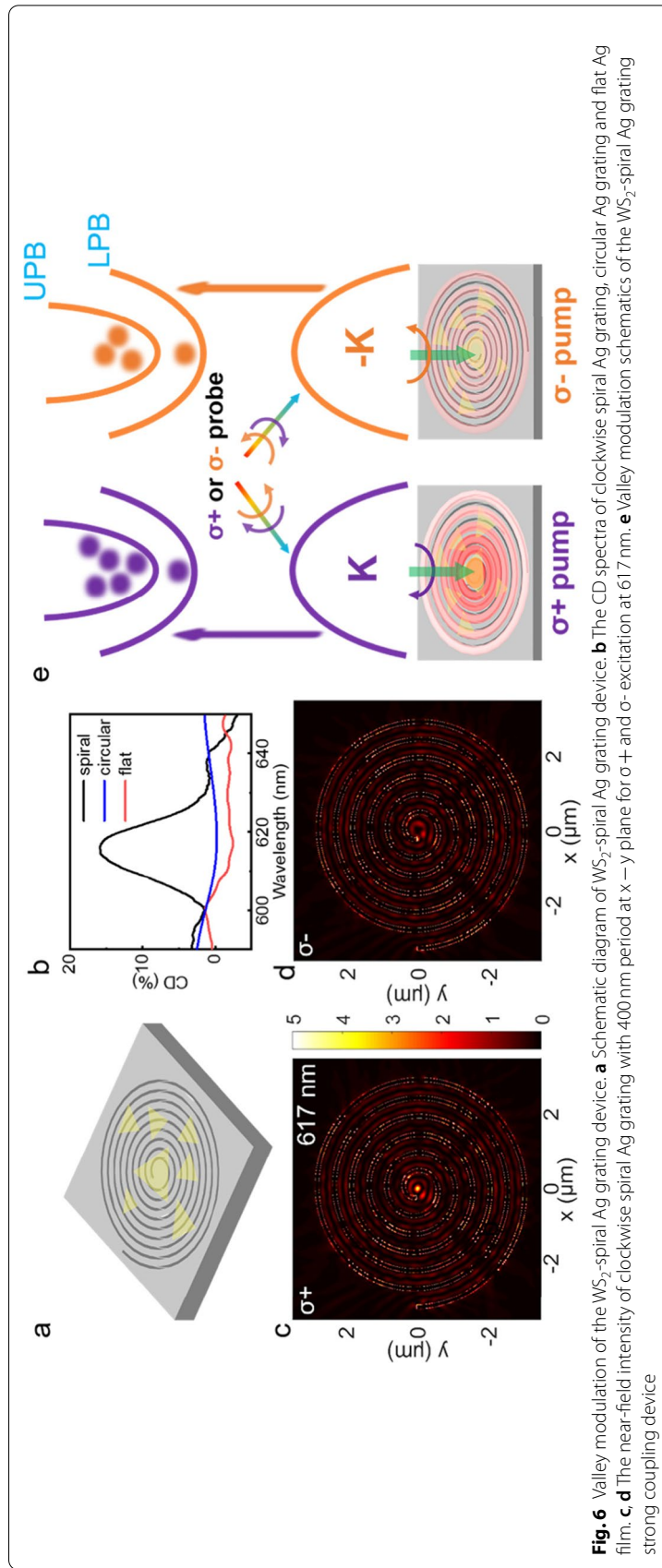


**Fig. 6** Valley modulation of the  $WS_2$ -spiral Ag grating device. **a** Schematic diagram of  $WS_2$ -spiral Ag grating device. **b** The CD spectra of clockwise spiral Ag grating, circular Ag grating and flat Ag film. **c, d** The near-field intensity of clockwise spiral Ag grating with 400 nm period at  $x - y$  plane for  $\sigma+$  and  $\sigma-$  excitation at 617 nm. **e** Valley modulation schematics of the  $WS_2$ -spiral Ag grating strong coupling device

which is also consistent with the simulated circular polarized steady state spectrum of the spiral Ag grating in Fig. S6. Thus, we confirm that the clockwise spiral grating can absorb more  $\sigma+$  light. Besides, the CD resonance of the clockwise spiral Ag gratings matches well with the transition energy of the A exciton in monolayer  $\text{WS}_2$ . Then, the corresponding near-field electric field distribution of the clockwise spiral grating for  $\sigma+$  and  $\sigma+$  light at the CD peak of 617 nm is simulated and plotted in Fig. 6c and d, which agrees with the experimental spectra well. As can be seen, only for  $\sigma+$  light, the excited SPPs can propagate along the clockwise spiral and focused to a strong hot-spot at the center of the spiral gratings (Fig. 6c). Conversely, without a focusing effect, a relatively weak electric field distribution is displayed for  $\sigma-$  light (Fig. 6d).

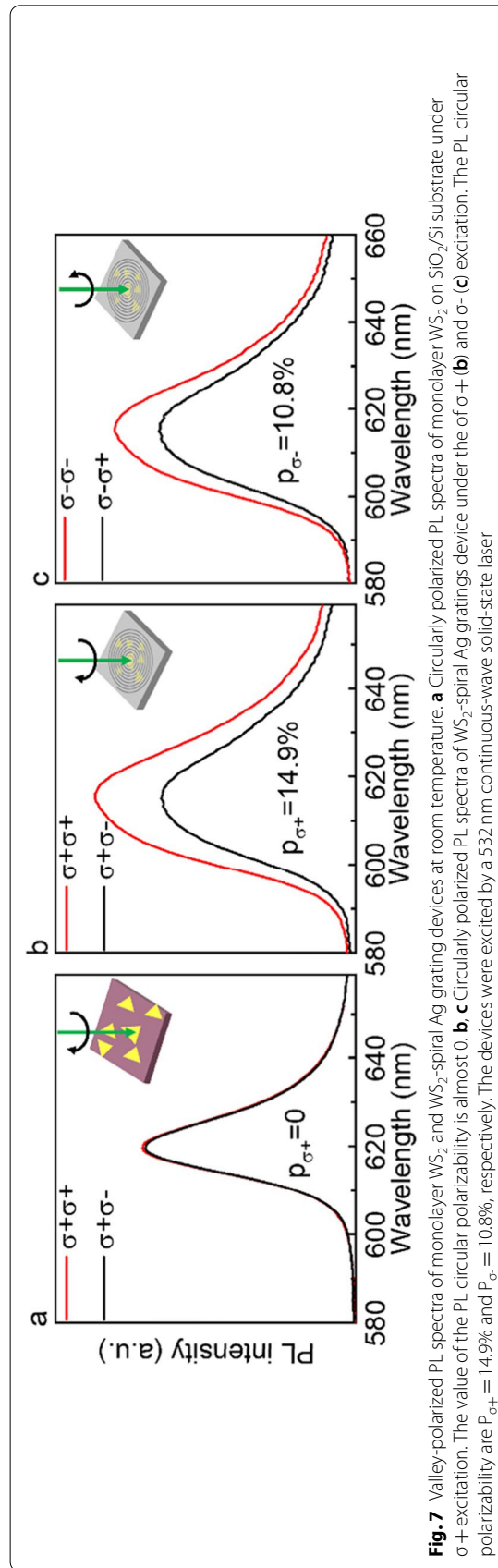
Then for the hybrid  $\text{WS}_2$ -spiral Ag grating device, circular polarized PL spectra was measured under excitation with a 532 nm laser. In the PL measurement system, a linear polarizer and a broadband quarter-wave plate (350–850 nm) were placed before the spectrometer to separate the  $\sigma+$  and  $\sigma-$  PL spectra (see details in [Methods](#)). To quantify the measurements, the circular PL polarization degree was defined as:

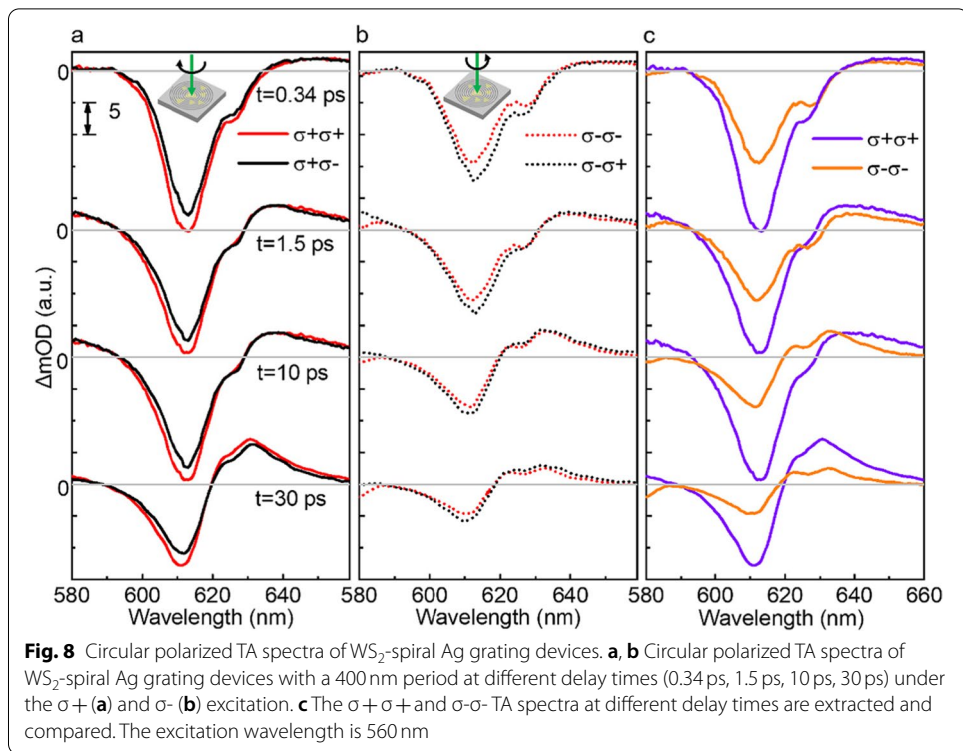
$$p_{\sigma+} = \frac{I_{++}-I_{+-}}{I_{++}+I_{+-}} \quad \text{and} \quad p_{\sigma-} = \frac{I_{--}-I_{-+}}{I_{--}+I_{-+}} \quad (2)$$

where  $I_{++}$  ( $I_{--}$ ) and  $I_{+-}$  ( $I_{-+}$ ) is the PL intensity component with the same and opposite polarization relative to the excitation.

First, the circular polarized PL spectra of monolayer  $\text{WS}_2$  on  $\text{SiO}_2/\text{Si}$  substrate were measured as reference. As shown in Fig. 7a, the bare  $\text{WS}_2$  shows an A-exciton PL peak at 620 nm with a full-width half maximum linewidth about 18 nm. Notably, there is almost no difference between  $\sigma+$  and  $\sigma-$  PL spectra under  $\sigma+$  excitation. Namely, the circular PL polarization of bare  $\text{WS}_2$  is close to 0%, which can be attribute to the fast intervalley scattering at room temperature as previously reported [57]. In contrast, the circular polarized PL spectra of the  $\text{WS}_2$ -spiral gratings hybrid device are shown in Fig. 7b and c. The first point worth noting is that the full-width half maximum linewidth is up to about 30 nm, which is much wider than that of bare  $\text{WS}_2$ . Although the Rabi splitting cannot be clearly observed, the highly reshaped PL spectra can still be considered as modulated by strong coupling effect, which is similar to the other TMDCs-SPPs strong coupling systems. More importantly, different circular polarization was observed under  $\sigma+$  and  $\sigma-$  excitation. The maximum value at the PL peak (615 nm) can be up to  $p_{\sigma+} = 14.9\%$  and  $p_{\sigma-} = 10.8\%$ , respectively. Thus, as compared to  $\sigma-$  excitation, a larger circular PL polarization can be achieved under  $\sigma+$  excitation, which confirms that an asymmetric modulation on the K and -K valleys are performed by the  $\text{WS}_2$ -clockwise spiral Ag gratings hybrid device.

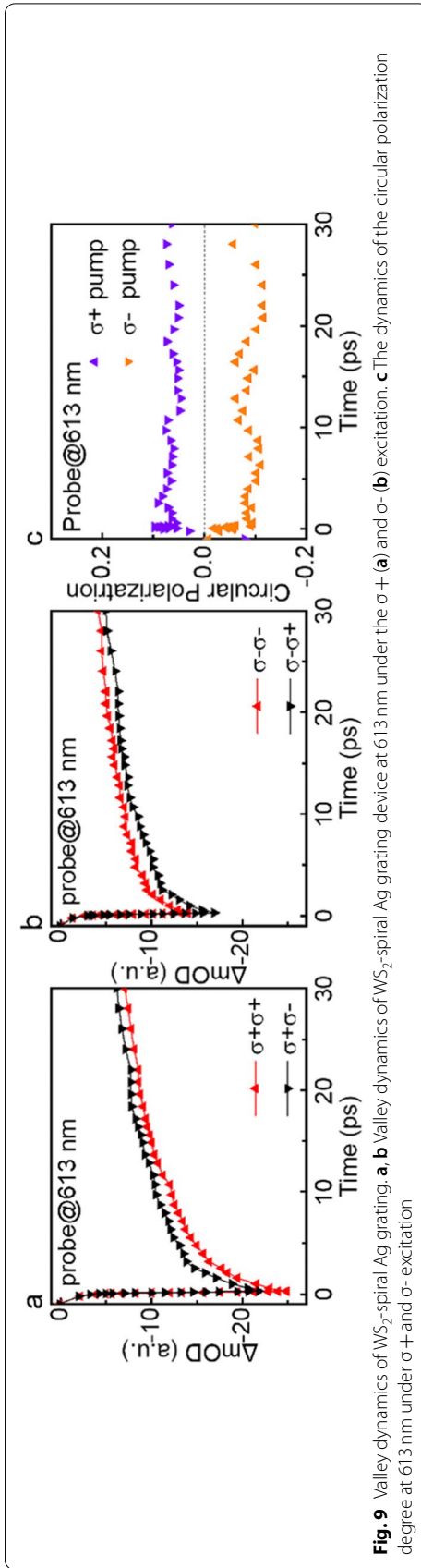
In order to further gain insight into the asymmetric valley control properties in the strong coupling devices, we carry out circular polarized TA spectroscopy again. The corresponding TA spectra on the  $\text{WS}_2$ -spiral Ag gratings hybrid device under  $\sigma+$  and  $\sigma-$  excitation are shown in Fig. 8a and b. Similar to  $\text{WS}_2$ -circular grating devices, two GSB signals, which can be assigned to the upper and lower bands, appear in all the pump-probe configurations, while the GSB from the uncoupled  $\text{WS}_2$  is not detectable. Furthermore, with respect to lower bands, the upper bands at 613 nm with a larger intensity is more apparent and there are no positive





signals overlapping in this range. Hence, we can compare the circular polarization degree at the upper bands more directly. As shown in Fig. 8a and b, the upper band acquires a larger signal intensity under SCP probe for  $\sigma+$  excitation; while the feature is just contrary for  $\sigma-$  excitation, in which a larger signal intensity was observed under OCP probe. Namely, the circular polarization at the upper band marked a complete reversal trend under  $\sigma+$  and  $\sigma-$  excitation. To visualize this feature, the circular polarization dynamics of the upper bands for  $\sigma+$  and  $\sigma-$  excitation are calculated from the valley dynamics (Fig. 9a and b) according to formula (1). As shown in Fig. 9c, the circular polarization degree with a value of  $P_{\sigma+} = 6\%$  and  $P_{\sigma-} = -8\%$  can be kept for an extremely long time (more than 20 ps). Compared with the bare  $WS_2$  sample, the circular polarization degree not only have a much longer lifetime, but also show opposite polarization degree under  $\sigma+$  and  $\sigma-$  excitation. Besides, the TA spectra for SCP probe under  $\sigma+$  and  $\sigma-$  excitation are extracted in Fig. 7c, where a huge difference can be observed. As can be seen, the GSB signals under  $\sigma+$  excitation is much bigger than that under  $\sigma-$  excitation over time. These results clearly indicate that valley polarization can be well preserved in the hybrid states and asymmetric control on the K and -K valley can be realized in such chiral strong coupling regime.

Finally, we would like to stress that the valley asymmetric modulation mechanism can be alternatively explained by the schematic diagram in Fig. 6e. According to simulation results in Fig. 6c, a stronger hot-spot can be generated only for  $\sigma+$  excitation in the clockwise spiral Ag grating and leads to an enhancement on the absorption of the hybrid system, resulting in a higher rate of  $\sigma+$  exciton-polaritons excited to K valley under  $\sigma+$  excitation. Conversely, there is no hot-spot generated



under  $\sigma^-$  excitation (Fig. 6d), thus the absorption cannot be enhanced in this case. Hence, selective absorption enhancement directly triggered the asymmetric modulation on the valleys. Besides, we conjecture that the remarkable long lifetime of the circular polarization degree can be caused by the inhibited valley depolarization in the strong coupling regime. In fact, the valley polarization lifetime is mainly determined by the exciton-polaritons relaxation and intervalley scattering rates. It has been demonstrated that robust valley polarization can be obtained even at room temperature in the cavity based strong coupling system. Due to the reduction of disorder scattering effect in strong coupling system, a 20 times longer polariton spin relaxation time [32] is estimated as compared to bare  $\text{WS}_2$ . Here, an even longer circular polarization lifetime was measured from the chiral strong coupling devices, which results in valley pseudospin retention at room temperature.

## Conclusion

To conclude, we have constructed various strong coupling systems by combining monolayer  $\text{WS}_2$  with different types of Ag gratings to investigate the polarization dynamics of the hybrid states using polarized TA spectroscopy. Firstly, we demonstrated that linear polarized PL can be tailored in  $\text{WS}_2$ -linear Ag grating device. The mechanism is understood by linear polarized pump-probe measurements, in which the TA signals from the strong coupled hybrid states can only be detected in TM mode and have an extremely long lifetime, resulting in robust linear polarization. But because the circular polarized light can be converted to linear polarized light by the linear Ag gratings, valley polarization cannot be detected in  $\text{WS}_2$ -linear Ag grating device. Hence circular Ag gratings were introduced to couple with  $\text{WS}_2$ . In  $\text{WS}_2$ -circular Ag grating devices, strong coupled hybrid states can also be achieved and a long valley polarization lifetime was observed. More importantly, to further improve the valley-addressable ability, chiral strong coupling was constructed in  $\text{WS}_2$ -spiral Ag grating devices. More than with a long lifetime, the valley polarization shows opposite behavior under  $\sigma^+$  and  $\sigma^-$  excitation. This is the reason why the PL circular polarization is different ( $P_{\sigma^+} = 14.9\%$  and  $P_{\sigma^-} = 10.8\%$ ). Our measurements suggest that the valley of the hybrid states can be controlled asymmetrically in chiral strong coupling regime. The above understanding on the valley dynamics of the coherent hybrid states could provide a new way to improve coding performance in valleytronic devices at room temperature.

## Methods

### Sample preparation

The Ag gratings with different periods were fabricated by electron beam lithography (EBL). Positive resist (950 PMMA AR-P 672.045) was first spin-coated (6000 rpm, 60 s) on the precleaned silicon substrate and annealed at 150 °C for 3 min, resulting in a PMMA film with thickness of 160 nm. Then the sample was patterned by EBL machine (Raith Pioneer Two, electron energy 10 KeV and beam current 150 pA) and developed in a conventional solution of MIBK:IPA = 1:3 for 3 min followed by isopropanol washing 1 min. After that, 200 nm silver and 5 nm  $\text{Al}_2\text{O}_3$  was deposited by electron-beam deposition (evaporation rate 2  $\text{\AA s}^{-1}$ ).



Finally, triangular monolayer WS<sub>2</sub> (purchased from SixCarbon Technology ShenZhen) was transferred to the gratings by wet method to finish the preparation of the WS<sub>2</sub>-Ag gratings coupling devices. Raman spectra of the monolayer WS<sub>2</sub> before the transfer was shown in Fig. S1.

#### Wet transfer method of monolayer WS<sub>2</sub> onto the gratings

The transfer process referred to Lu's work [58]. First, 1.5 g of PVP (Alfa Aesar, average MW 58000), 1.5 mL of NVP (J&K, 99.5%), 0.75 mL of deionized water, and 7 mL of ethanol was mixed in a vial for 10 min at room temperature. The solution was spin-coated on the triangular monolayer WS<sub>2</sub> flakes adhered to the SiO<sub>2</sub>/Si substrate at 2000 rpm for 1 min and then baked at 70 °C for 1 min. After that, a 9 wt% PVA film (Alfa Aesar, 98 – 99% hydrolyzed, high molecular weight) was spin-coated on top of the sample at 2000 rpm for 1 min. The PVA/NVP film with triangular monolayer WS<sub>2</sub> flakes was peeled off from the SiO<sub>2</sub>/Si substrate and then attached to the Ag-grating substrate through the electrostatic force. Finally, the WS<sub>2</sub>-grating devices were washed in deionized water for 1 h to remove the PVA/NVP film. The process is shown schematically in Fig. S2a. The SEM images of the multiple WS<sub>2</sub>-gratings devices were shown in Fig. S3.

#### Optical measurements

The polarized PL spectra was excited by a 532 nm continuous-wave solid-state laser in the TM direction. The PL emission was collected by a fiber-spectrometer (AvaSpec-ULS2048XL-EVO). A polarizer is set in front of the spectrometer for the polarization analysis, where the TE and TM mode are defined as perpendicular (90°) and parallel (0°) to the long axis of the gratings. For the reflection spectra, the incident white light was set in the TE direction and the reflected light was collected under the normal incidence by the same fiber-spectrometer.

The linear polarized femtosecond transient absorption (TA) experiments were performed using a 100 fs laser pump-probe setup. A mode-locked titanium sapphire laser/amplifier system (Solstice, Spectra-Physics) was used. The output fundamental pulses centered at 800 nm with a repetition rate of 500 Hz and a pulse width of 100 fs was split into two laser beams. The stronger part was sent to an optical parametric amplifier (TOPAS C, Spectra-Physics) to generate pump laser at 560 nm. The other beam with lower energy was focused on a 5 mm thick sapphire crystal to generate broad white-light continuum (from 450 nm to 800 nm) as probe beam. The pump and probe laser were collinear by a beam splitter cube and focused on the same position of the sample at normal incidence. The diameter of the probe spot is about 5 μm under optimized focusing, while the pump spot is a little larger due to the chromatic aberrations. The delay time between the pump and the probe pulses were controlled by a motorized mechanical delay stage (DL325, Newport). Finally, the reflected probe light from the sample was collected by the same objective and sent to a highly sensitive spectrometer (Avantes-ULS2048CL-EVO). The group velocity dispersion of the whole experimental system was compensated by a chirp program.

### Abbreviations

TMDCs: Two-dimensional transition metal dichalcogenides; TA: Transient absorption; PL: Photoluminescence; SPPs: Surface plasmon polaritons; GSB: Ground state bleaching; SCP: Same circular polarization; OCP: Opposite circular polarization; PIA: Photoinduced absorption.

### Supplementary Information

The online version contains supplementary material available at <https://doi.org/10.1186/s43074-022-00049-1>.

**Additional file 1: Figure S1.** Raman spectra of monolayer WS<sub>2</sub> on SiO<sub>2</sub>/Si substrate (show in the inserted optical image) at the excitation light of 532 nm. The scale bar is 5 μm. **Figure S2.** (a) Schematic diagrams of the fabrication process of WS<sub>2</sub>-Ag grating of devices. (b) The SEM image of the linear Ag grating. (c) The optical image of the monolayer WS<sub>2</sub>-linear Ag grating device. The scale bar is 1 μm. **Figure S3.** The SEM images of WS<sub>2</sub>-linear Ag grating (a)- (b), WS<sub>2</sub>-circular Ag grating (c)- (d) and WS<sub>2</sub>-spiral Ag grating (e)- (f) devices. The white scale bar is 10 μm, and the black scale bar is 1 μm. **Figure S4.** (a) The SEM image of the linear Ag gratings. (b) cross-sectional image of the linear Ag gratings obtained with focused ion beam (FIB) etching. **Figure S5.** Raman spectra of monolayer WS<sub>2</sub> on Ag flat or gratings at the excitation light of 532 nm. The scale bar is 5 μm. **Figure S6.** Simulation of the circular polarization of multiple Ag gratings at the center of the samples.

### Acknowledgements

Not applicable.

### Authors' contributions

L.-Y. Zhao, H. Wang, H.-Y. Wang, Q. Zhou and H.-B. Sun conceived the initial idea, L.-Y. Zhao, X.-L. Zhang, T. Cui, L. Wang, T.-Y. Liu, Y.-X. Han, Y. Luo, Y.-Y. Tue and M.-S. Song performed the experiments. L.-Y. Zhao analyzed the data. H. Wang, H.-Y. Wang, Q. Zhou, and H.-B. Sun discussed the results and supervised the project. All authors read and approved the final manuscript.

### Funding

This work was supported by the National Key Research and Development Program of China and the National Natural Science Foundation of China (NSFC) under Grants 21903035, 22073037, 21773087, 12074141, 61960206003 and Jilin Provincial Science and Technology Development Project (20210509038RQ).

### Availability of data and materials

The datasets used and/or analysed during the current study are available from the corresponding author on reasonable request.

### Declarations

#### Competing interests

The authors declare that they have no competing interests.

#### Author details

<sup>1</sup>State Key Laboratory of Integrated Optoelectronics, College of Electronic Science and Engineering, Jilin University, Changchun 130012, China. <sup>2</sup>State Key Laboratory of Superhard Materials, College of Physics, Jilin University, Changchun 130012, China. <sup>3</sup>State Key Laboratory of Precision Measurement Technology and Instruments, Department of Precision Instrument, Tsinghua University, Haidian, Beijing 100084, China.

Received: 8 December 2021 Accepted: 4 February 2022

Published online: 11 February 2022

### References

1. Mak KF, He K, Shan J, Heinz TF. Control of valley polarization in monolayer MoS<sub>2</sub> by optical helicity. *Nat Nanotechnol.* 2012;7:494–8.
2. Li Y, Rao Y, Mak KF, You Y, Wang S, Dean CR, et al. Probing symmetry properties of few-layer MoS<sub>2</sub> and h-BN by optical second-harmonic generation. *Nano Lett.* 2013;13:3329–33.
3. Podzorov V, Gershenson ME, Kloc C, Zeis R, Bucher E. High-mobility field-effect transistors based on transition metal dichalcogenides. *Appl Phys Lett.* 2004;84:3301–3.
4. Yu L, Lee Y-H, Ling X, Santos EJG, Shin YC, Lin Y, et al. Graphene/MoS<sub>2</sub> hybrid technology for large-scale two-dimensional electronics. *Nano Lett.* 2014;14:3055–63.
5. Yang LY, Chen WB, McCreary KM, Jonker BT, Lou J, Crooker SA. Spin coherence and dephasing of localized electrons in monolayer MoS<sub>2</sub>. *Nano Lett.* 2015;15:8250–4.
6. Yu H, Cui X, Xu X, Yao W. Valley excitons in two-dimensional semiconductors. *Natl Sci Rev.* 2015;2:57–70.
7. Selig M, Katsch F, Schmidt R, de Vasconcellos SM, Bratschitsch R, Malic E, et al. Ultrafast dynamics in monolayer transition metal dichalcogenides: interplay of dark excitons, phonons, and intervalley exchange. *Phys Rev Res.* 2019;1:022007.

8. Xu S, Si C, Li Y, Gu B-L, Duan W. Valley depolarization dynamics in monolayer transition-metal dichalcogenides: role of the satellite valley. *Nano Lett.* 2021;21:1785–91.
9. Amo A, Liew TCH, Adrados C, Houdre R, Giacobino E, Kavokin AV, et al. Exciton-polariton spin switches. *Nat Photonics.* 2010;4:361–6.
10. Mak KF, McGill KL, Park J, McEuen PL. The valley hall effect in MoS<sub>2</sub> transistors. *Science.* 2014;344:1489–92.
11. Radisavljevic B, Radenovic A, Brivio J, Giacometti V, Kis A. Single-layer MoS<sub>2</sub> transistors. *Nat Nanotechnol.* 2011;6:147–50.
12. Ling H, Li R, Davoyan AR. All van der Waals integrated nanophotonics with bulk transition metal dichalcogenides. *ACS Photonics.* 2021;8:721–30.
13. Geim AK, Grigorieva IV. Van der Waals heterostructures. *Nature.* 2013;499:419–25.
14. Pei J, Yang J, Yildirim T, Zhang H, Lu Y. Many-body complexes in 2D semiconductors. *Adv Mater.* 2019;31:1706945.
15. Yue Y-Y, Wang Z, Wang L, Wang H-Y, Chen Y, Wang D, et al. Many-particle induced band renormalization processes in few- and mono-layer MoS<sub>2</sub>. *Nanotechnology.* 2021;32:135208.
16. Yang GC, Shen QX, Niu YJ, Wei H, Bai BF, Mikkelsen MH, et al. Unidirectional, ultrafast, and bright spontaneous emission source enabled by a hybrid plasmonic nanoantenna. *Laser Photonics Rev.* 2020;14:8.
17. Amani M, Lien D-H, Kiriya D, Xiao J, Azcatl A, Noh J, et al. Near-unity photoluminescence quantum yield in MoS<sub>2</sub>. *Science.* 2015;350:1065–8.
18. Kasprzak J, Richard M, Kundermann S, Baas A, Jeambrun P, Keeling JMJ, et al. Bose–Einstein condensation of exciton polaritons. *Nature.* 2006;443:409–14.
19. Deng H, Haug H, Yamamoto Y. Exciton-polariton Bose–Einstein condensation. *Rev Mod Phys.* 2010;82:1489–537.
20. Ye Y, Wong ZJ, Lu X, Ni X, Zhu H, Chen X, et al. Monolayer excitonic laser. *Nat Photonics.* 2015;9:733–7.
21. Wu S, Buckley S, Schaibley JR, Feng L, Yan J, Mandrus DG, et al. Monolayer semiconductor nanocavity lasers with ultralow thresholds. *Nature.* 2015;520:69–72.
22. Georgiou K, Michetti P, Gai L, Cavazzini M, Shen Z, Lidzey DG. Control over energy transfer between fluorescent BODIPY dyes in a strongly coupled microcavity. *ACS Photonics.* 2018;5:258–66.
23. Liu S, Wu YZ, Liu X, del Aguila AG, Xuan FY, Chaturvedi A, et al. Light-matter interactions in high quality manganese-doped two-dimensional molybdenum diselenide. *Sci China Mater.* 2021;64:2507–18.
24. Chen Y-J, Cain JD, Stanev TK, Dravid VP, Stern NP. Valley-polarized exciton-polaritons in a monolayer semiconductor. *Nat Photonics.* 2017;11:431–5.
25. Flatten LC, Coles DM, He Z, Lidzey DG, Taylor RA, Warner JH, et al. Electrically tunable organic-inorganic hybrid polaritons with monolayer WS<sub>2</sub>. *Nat Commun.* 2017;8(1):1–5.
26. Mey O, Wall F, Schneider LM, Gunder D, Walla F, Soltani A, et al. Enhancement of the monolayer tungsten disulfide exciton photoluminescence with a two-dimensional material/air/gallium phosphide in-plane microcavity. *ACS Nano.* 2019;13:5259–67.
27. Lee B, Liu W, Naylor CH, Park J, Malek SC, Berger JS, et al. Electrical tuning of exciton-plasmon polariton coupling in monolayer MoS<sub>2</sub> integrated with plasmonic nanoantenna lattice. *Nano Lett.* 2017;17:4541–7.
28. Wen J, Wang H, Wang W, Deng Z, Zhuang C, Zhang Y, et al. Room-temperature strong light-matter interaction with active control in single plasmonic nanorod coupled with two-dimensional atomic crystals. *Nano Lett.* 2017;17:4689–97.
29. Cuadra J, Baranov DG, Wersall M, Verre R, Antosiewicz TJ, Shegai T. Observation of tunable charged exciton polaritons in hybrid monolayer WS<sub>2</sub>-plasmonic nanoantenna system. *Nano Lett.* 2018;18:1777–85.
30. Shan HY, Yu Y, Wang XL, Luo Y, Zu S, Du BW, et al. Direct observation of ultrafast plasmonic hot electron transfer in the strong coupling regime. *Light Sci Appl.* 2019;8(1):1–9.
31. Wang JJ, Li H, Ma YT, Zhao MX, Liu WZ, Wang B, et al. Routing valley exciton emission of a WS<sub>2</sub> monolayer via delocalized Bloch modes of in-plane inversion-symmetry-broken photonic crystal slabs. *Light Sci Appl.* 2020;9:8.
32. Dufferwiel S, Lyons TP, Solnyshkov DD, Trichet AAP, Withers F, Schwarz S, et al. Valley-addressable polaritons in atomically thin semiconductors. *Nat Photonics.* 2017;11:497–501.
33. Sun Z, Gu J, Ghazaryan A, Shotan Z, Considine CR, Dollar M, et al. Optical control of room-temperature valley polaritons. *Nat Photonics.* 2017;11:491–6.
34. Lin HT, Chang CY, Cheng PJ, Li MY, Cheng CC, Chang SW, et al. Circular dichroism control of tungsten diselenide (WSe<sub>2</sub>) atomic layers with plasmonic metamolecules. *ACS Appl Mater Interfaces.* 2018;10:15996–6004.
35. Hu G, Hong X, Wang K, Wu J, Xu H-X, Zhao W, et al. Coherent steering of nonlinear chiral valley photons with a synthetic Au-WS<sub>2</sub> metasurface. *Nat Photonics.* 2019;13:467–72.
36. Sun L, Wang C-Y, Krasnok A, Choi J, Shi J, Gomez-Diaz JS, et al. Separation of valley excitons in a MoS<sub>2</sub> monolayer using a subwavelength asymmetric groove array. *Nat Photonics.* 2019;13:180–4.
37. Qiao Z, Wan Z, Xie G, Wang J, Qian L, Fan D. Multi-vortex laser enabling spatial and temporal encoding. *Photonix.* 2020;1:13.
38. Qian Z, Shan L, Zhang X, Liu Q, Ma Y, Gong Q, et al. Spontaneous emission in micro- or nanophotonic structures. *Photonix.* 2021;2:21.
39. Wang J, Li H, Ma Y, Zhao M, Liu W, Wang B, et al. Routing valley exciton emission of a WS<sub>2</sub> monolayer via delocalized Bloch modes of in-plane inversion-symmetry-broken photonic crystal slabs. *Light Sci Appl.* 2020;9:148.
40. Liu WZ, Wang B, Zhang YW, Wang JJ, Zhao MX, Guan F, et al. Circularly polarized states spawning from bound states in the continuum. *Phys Rev Lett.* 2019;123:6.
41. Puchert RP, Hofmann FJ, Angerer HS, Vogelsang J, Bange S, Lupton JM. Linearly polarized electroluminescence from MoS<sub>2</sub> monolayers deposited on metal nanoparticles: toward tunable room-temperature single-photon sources. *Small.* 2021;17:8.
42. Li JL, Nie CB, Sun FY, Tang LL, Zhang ZJ, Zhang JD, et al. Enhancement of the photoresponse of monolayer MoS<sub>2</sub> photodetectors induced by a nanoparticle grating. *ACS Appl Mater Interfaces.* 2020;12:8429–36.
43. Shi J, Liang W-Y, Raja SS, Sang Y, Zhang X-Q, Chen C-A, et al. Plasmonic enhancement and manipulation of optical nonlinearity in monolayer tungsten disulfide. *Laser Photonics Rev.* 2018;12:1800188.

44. Li ZW, Li Y, Han TY, Wang XL, Yu Y, Tay B, et al. Tailoring MoS<sub>2</sub> exciton-plasmon interaction by optical spin-orbit coupling. *ACS Nano*. 2017;11:1165–71.
45. Chervy T, Azzini S, Lorchat E, Wang S, Gorodetski Y, Hutchison JA, et al. Room temperature chiral coupling of valley excitons with spin-momentum locked surface plasmons. *ACS Photonics*. 2018;5:1281–7.
46. Li Z, Liu C, Rong X, Luo Y, Cheng H, Zheng L, et al. Tailoring MoS<sub>2</sub> valley-polarized photoluminescence with super chiral near-field. *Adv Mater*. 2018;30(34):1801908.
47. Guddala S, Bushati R, Li M, Khanikaev AB, Menon VM. Valley selective optical control of excitons in 2D semiconductors using a chiral metasurface invited. *Opt Mater Express*. 2019;9:536–43.
48. Wu ZL, Li JG, Zhang XT, Redwing JM, Zheng YB. Room-temperature active modulation of valley dynamics in a monolayer semiconductor through chiral Purcell effects. *Adv Mater*. 2019;31:9.
49. Li H, Wang J, Ma Y, Chu J, Cheng X, Shi L, et al. Enhanced directional emission of monolayer tungsten disulfide (WS<sub>2</sub>) with robust linear polarization via one-dimensional photonic crystal (PhC) slab. *Nanophotonics*. 2020;9:4337–45.
50. Wang L, Li Q, Wang HY, Huang JC, Zhang R, Chen QD, et al. Ultrafast optical spectroscopy of surface-modified silicon quantum dots: unraveling the underlying mechanism of the ultrabright and color-tunable photoluminescence. *Light Sci Appl*. 2015;4:245.
51. Wang H, Wang H-Y, Bozzola A, Toma A, Panaro S, Raja W, et al. Dynamics of strong coupling between J-aggregates and surface plasmon polaritons in subwavelength hole arrays. *Adv Funct Mater*. 2016;26:6198–205.
52. Wang H, Wang HY, Chen QD, Xu HL, Sun HB, Huang FC, et al. Hybrid-state dynamics of dye molecules and surface plasmon polaritons under ultrastrong coupling regime. *Laser Photonics Rev*. 2018;12:1700176.
53. Schmidt R, Berghäuser G, Schneider R, Selig M, Tonndorf P, Malić E, et al. Ultrafast coulomb-induced intervalley coupling in atomically thin WS<sub>2</sub>. *Nano Lett*. 2016;16:2945–50.
54. Andreou AG, Kalayjian ZK. Polarization imaging: principles and integrated polarimeters. *IEEE Sensors J*. 2002;2:566–76.
55. Bai J, Yao Y. Highly efficient anisotropic chiral plasmonic metamaterials for polarization conversion and detection. *ACS Nano*. 2021;15:14263–74.
56. Osorio CI, Coenen T, Brenny BJM, Polman A, Koenderink AF. Angle-resolved cathodoluminescence imaging polarimetry. *ACS Photonics*. 2016;3:147–54.
57. Berghäuser G, Bernal-Villamil I, Schmidt R, Schneider R, Niehues I, Erhart P, et al. Inverted valley polarization in optically excited transition metal dichalcogenides. *Nat Commun*. 2018;9:971.
58. Lu ZX, Sun LF, Xu GC, Zheng JY, Zhang Q, Wang JY, et al. Universal transfer and stacking of chemical vapor deposition grown two-dimensional atomic layers with water-soluble polymer mediator. *ACS Nano*. 2016;10:5237–42.

## Publisher's Note

Springer Nature remains neutral with regard to jurisdictional claims in published maps and institutional affiliations.

Submit your manuscript to a SpringerOpen<sup>®</sup> journal and benefit from:

- Convenient online submission
- Rigorous peer review
- Open access: articles freely available online
- High visibility within the field
- Retaining the copyright to your article

---

Submit your next manuscript at ► [springeropen.com](https://www.springeropen.com)

---